Indian J Phys
https://doi.org/10.1007/s12648-023-03028-9

ORIGINAL PAPER

Facile synthesis and physical properties of magnesium dititanate nanoparticles for antibacterial applications

S Elnobi[1]*, A A Abuelwafa[2]*, M S Abd El-sadek[3,4] and H S Wasly[5]

[1]Physics Department, Faculty of Science, South Valley University, Qena 83523, Egypt

[2]Nano and Thin Film Laboratory, Physics Department, Faculty of Science, South Valley University, Qena 83523, Egypt

[3]Physics Department, Faculty of Science, Galala University, Galala City, Egypt

[4]Nanomaterials Laboratory, Physics Department, Faculty of Science, South Valley University, Qena 83523, Egypt

[5]Mining, Metallurgy and Petroleum Engineering Department, Faculty of Engineering, Al-Azhar University, Qena, Egypt

Received: 21 July 2023 / Accepted: 06 November 2023

Abstract: The modified aqueous co-precipitation approach was used to successfully manufacture magnesium dititanate ($MgTi_2O_5$) nanoparticles. Thermogravimetric analysis/differential scanning calorimetry (TG/DSC) was used to clearly reveal the thermal stability. Moreover, pseudobrookite structure, and surface morphology of $MgTi_2O_5$ nanoparticles were determined using X-ray diffraction (XRD), transmission electron microscope (TEM), and Fourier-transform infrared (FT-IR), and scanning electron microscope (SEM) techniques, respectively. The average size of the crystallites calculated by Scherer approach was compared to Williamson-Hall and TEM images results. The optical band gap of $MgTi_2O_5$ nanoparticles was found to be 3.81 eV for direct transitions. The effect of temperature on the conductivity of DC electricity was tested between the rages 303–503 K. The data on antibacterial activity showed that $MgTi_2O_5$ nanoparticles were antimicrobial and stopped the test microorganisms from growing. These findings revealed that $MgTi_2O_5$ will be extensively promising in environmental pollution control and antibacterial research.

Keywords: $MgTi_2O_5$; Pseudobrookite; Electrical properties; Optical properties; Antibacterial

Introduction

Due to their low bulk thermal expansion, the pseudobrookite-type crystal structure-based pigments were developed to provide heat-resistant coloring agents for thermoplastics, industrial paints, and other low-temperature applications. Their various ceramics that have pseudobrookite-type structures (such as $MgTi_2O_5$ and Fe_2TiO_5) were studied. $MgTi_2O_5$ with a pseudobrookite-type system has potential applications owing to its good mechanical properties, good thermal stability, and high thermal shock resistance [1–7]. Furthermore, $MgTi_2O_5$ has a high refractive index, high permittivity, low cost, and no dielectric loss [8, 9]. Many techniques, including solid-state reaction, conventional high-temperature, thermal decomposition of precursors, simultaneous hydrolysis, sol–gel method, and co-precipitation, sol–gel, and other methods, have been used in recent years to synthesize $MgTi_2O_5$ like-pseudobrookite structure materials [10–18].

Pseudobrookite materials have attracted considerable attention as a potential photocatalyst material that might be extensively employed in environmental pollution remediation and antibacterial research [18, 19]. $MgTi_2O_5$ has been used for diesel particulate filters with high-temperature steadiness. In addition, $MgTi_2O_5$ has been utilized as a porous ceramic membrane and can be used as a white pigment, electrical resistor, catalyst, water purification filter, and photocatalyst [10, 14]. There has been considerable interest in the development of antibacterial materials and coatings for many years. This interest is growing due to the growth of antibacterial-resistant bacteria over the last decade and the prevalence of healthcare-associated illnesses (HCAIs). Anti-anti-bacterial may be used to minimize infection rates in a patient setting, but they also be used in waste-water treatment and the efficient production of clean drinking water via the augmentation of sun

*Corresponding author, E-mail: sahar.elnobi@sci.svu.edu.eg; amr.abuelwafa@sci.svu.edu.eg

Published online: 01 February 2024

sterilization[20–22]. The research gap for the study of the antimicrobial activities of $MgTi_2O_5$ nanoparticles is significant. There is no published research on this topic and the potential antimicrobial properties of $MgTi_2O_5$ nanoparticles have not been investigated at all. In addition to these specific research gaps, there is also a need to develop new methods for synthesizing and characterizing $MgTi_2O_5$ nanoparticles. This would enable researchers to produce $MgTi_2O_5$ nanoparticles with controlled size, shape, and surface properties, which is important for optimizing their antimicrobial activity. Further research is needed to address the research gaps identified above and to develop $MgTi_2O_5$ nanoparticles with optimal antimicrobial activity and safety.

As a result, the current study's purpose is to synthesize $MgTi_2O_5$ nanoparticles using co-precipitation, which is a quick, simple, ecologically friendly, and practical method. XRD, TG/DSC, FT-IR, SEM, EDX, TEM, UV–Vis spectroscopy, and DC measurements were used to analyze the structure, shape, and electrical conductivity of the $MgTi_2O_5$ nanoparticles generated, respectively. Antibacterial properties of $MgTi_2O_5$ nanoparticles were researched and evaluated.

Experimental details

Preparation of $MgTi_2O_5$ nanoparticles

The building blocks for making magnesium dititanate ($MgTi_2O_5$) were magnesium chloride ($MgCl_2$) and titanium tetrachloride ($TiCl_4$). Isopropanol, hydrogen peroxide (H_2O_2), and ammonia solutions (NH_4OH) are also utilized. All the reaction materials were used as received without further purification. $MgCl_2$ and $TiCl_4$ were both dissolved in 100 ml of distilled water and isopropanol, respectively, at a concentration of 0.2 mol of each. A new homogeneous solution was created by combining the two produced solutions. Next, 15 ml of hydrogen peroxide, 20 ml of ammonia, and 165 ml of distilled water are combined to make a solution. A precipitate was generated and filtered after adding $MgCl_2$ and $TiCl_4$ to the prepared solution combination drop by drop. The resulting precipitate was separated by centrifuging and washing it repeatedly with distilled water. The material was then dried in an oven set at 75 °C for six hours and calcined for approximately an hour in a muffle furnace set at around 800 °C. The reactions that go into making $MgTi_2O_5$ nanoparticles are shown in Scheme 1.

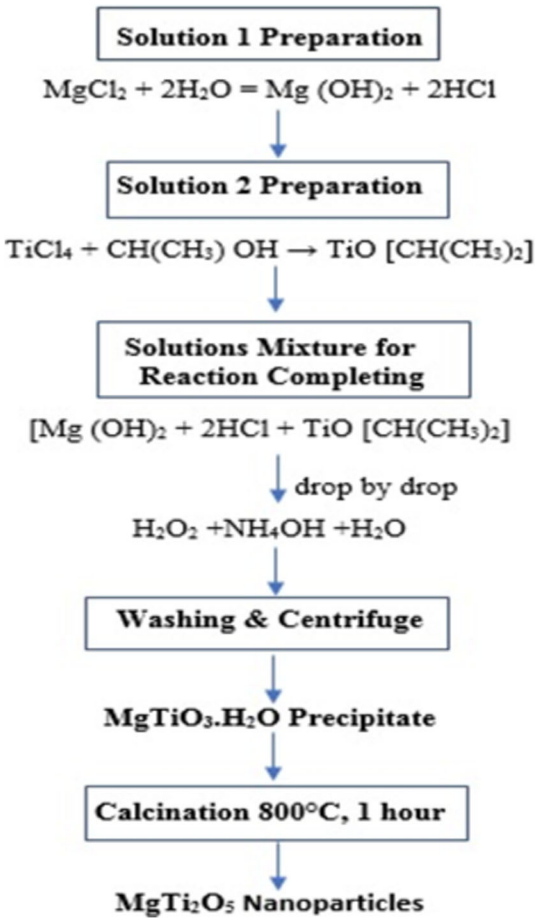

Scheme 1 Schematic steps of $MgTi_2O_5$ nanoparticles synthesis

Characterization

Thermal analysis was carried out using LINSEIS STA PT-1000 to investigate the thermal stability of $MgTi_2O_5$ nanoparticles (about 25 mg of the sample was taken and heated at a rate of 10 °C/min to 800 °C). The XRD pattern was recorded for $MgTi_2O_5$ nanoparticles using X-ray diffractometry (Brucker AXS D8 Advance X-ray diffractometer). The sample morphology was investigated using SEM (model JEOL-JSM-IT200). TEM (JEOL, JEMA 2100) equipped with an EDX detector was used to examine crystallites for their form, size, and elemental composition. Chemical characterization of $MgTi_2O_5$ nanoparticles was investigated using an FT-IR spectrometer (JASCO, Model 6100) at room temperature in the 400–4000 cm^{-1} range with a resolution of 4 cm^{-1}. Using a diffuse reflectance UV–Vis spectrophotometer (JASCO 670 UV–Vis-NIR spectrophotometer) with an integrating sphere and a spectral reflectance standard across the range (200–800) nm Discs containing $MgTi_2O_5$ nanoparticles were compressed (at 5 tons) and then sintered at 1000 °C in the air for 30

Table 1 Minimum inhibitory concentration (MIC)

Gram (+ ve) bacteria *E. faecalis*	Gram (− ve) bacteria *E. coli*	Sample
25 mg/ml	25 mg/ml	$MgTi_2O_5$ Nanoparticles

min in order to investigate their electrical conductivity. The silver paste was used to make electrical connections. The DC electrical conductivity of the sample was measured using an electrometer (KEITHLEY 6517A) linked directly to the sample. The temperature of system was regulated in a specific range (303–503 K) with an accuracy of roughly ± 1 K using a temperature controller.

Antibacterial activity

The antimicrobial effectiveness of the obtained $MgTi_2O_5$ nanoparticles was investigated. The tested strains of bacteria were *Escherichia coli* (*E. coli*) bacteria (ATCC25922, gram-negative) and *Enterococcus faecalis* bacteria (ATC29212, Gram-positive). Muller–Hinton agar was used as a culture medium at pH = 7.3 ± 0.1, and then an incubation period of 24–48 h at 37 °C was carried out for the plates [23, 24]. Antibacterial efficiency was specified for the mentioned bacteria by the method of paper disc assay. The Whatman filter paper disc was sterilized using an autoclave at 121 °C for 20 min. To determine the MIC (minimum inhibitory concentration), a concentration of the $MgTi_2O_5$ nanoparticles was used, as shown in Table 1. The sterile discs were impregnated with the determined concentration of $MgTi_2O_5$ (25 mg/mL) and then diluted [24]. Agar plates were injected into the broth of the used microorganisms with a uniform concentration of approximately 1.5×10^8 CFU ml^{-1}. Chloro-amphenicol with a concentration of 50 mg/mL was applied against the used bacteria as an effective control. The diameter of the growth inhibition halos caused by the examined compounds was calculated and expressed in millimeters. The applied tests were checked in triplicate.

Results and discussion

Structural properties

The thermal stability of $MgTi_2O_5$ nanoparticles is investigated using TGA and DTA curves, as displayed in Fig. 1. The weight loss from room temperature to 150 °C is about 28%, and the endothermic peak around 82 °C could be related to the presence of adsorbed water and the structural hydroxyl groups. The exothermic sharp peak at 107 °C corresponds to the beginning of the decomposition of the residual organic precursor groups of Ti-tetrachloride and Mg-chloride. In the range of 150–500 °C, the mass change is about 7% and has a broad exothermic peak around 285 °C. That is attributed to the completed decomposition of the organic deposits and the starting of OH-group (dehydroxylation) removal; this means that $MgTi_2O_5$ phase formation begins [25, 26]. The exothermic peak at 509 °C shows the crystallization of the obtained powders. The small mass loss in the range 500–800 °C is accompanied by an action that can be referred to as the elimination of OH-group decomposition [7, 25]. It is obvious that the formation and crystallization of the $MgTi_2O_5$ compound occur [1, 12, 27, 28].

The XRD pattern of $MgTi_2O_5$ nanoparticles synthesized by precipitation technique is shown in Fig. 2. Comparing the XRD pattern to the standard database (JCPDS) revealed that it belonged to the $MgTi_2O_5$ compound. The phase analysis of the sample is done using X'pert high score plus program, and the result is matched with JCPDS 82-1125. The estimated unit cell parameters and their values are indicated in Table 2. From Fig. 2, it can be indicated that there are no other phases presented (i.e., pure orthorhombic phase $MgTi_2O_5$). That means that no other impurity peaks are detected. The average crystallite size L is calculated using the Debye–Scherrer formula [29–33].

$$L = \frac{K\lambda}{\beta\cos\theta} \tag{1}$$

where, θ is Bragg's angle, β is the FWMH (full width at half maximum) in radian, λ = 0.15406 nm is the wavelength of the used X-ray, and K = 0.94 is constant. The two key factors responsible for the change in peak broadening in an XRD pattern are crystallite size and lattice strain. The dispersion of lattice constants due to defects in the crystal structure is quantified using the Williamson-Hall (W–H) technique is used to assess the L and assuming that two components contribute to peak broadening and are independent of one another, the observed peak width is expressed as the sum of L and H, as shown in the following W–H equation [34]:

$$\beta_{hkl}\cos\theta = \frac{K\lambda}{L} + 4\varepsilon\sin\theta \tag{2}$$

Figure 3 depicts a plot with $4\sin\theta$ along the x-axis and $\beta_{hkl}\cos\theta$ along the y-axis for $MgTi_2O_5$ nanoparticles. L is determined from the y-intercept and from the slope of Fig. 3 based on the linear fit to the data. The quantity of defects and vacancies (dislocation density, δ) in the $MgTi_2O_5$ can be determined using L and the following equation [33–35]:

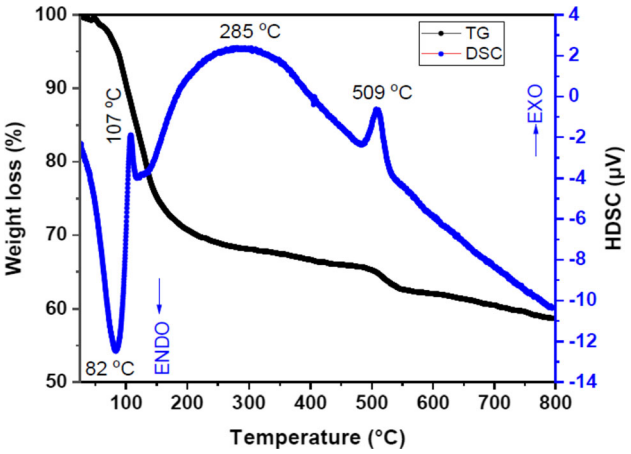

Fig. 1 Thermal analysis (ATG/DSC) for $MgTi_2O_5$ nanoparticles

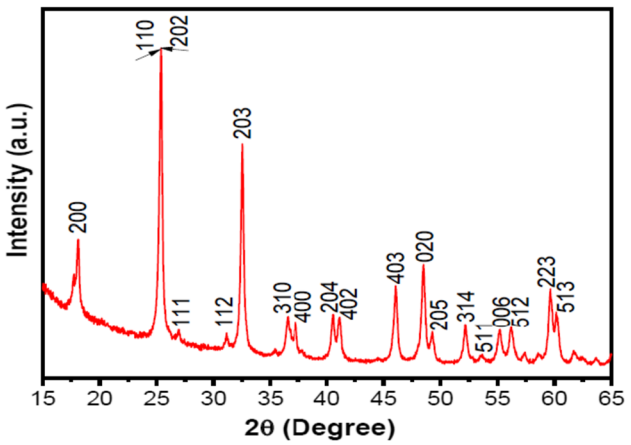

Fig. 2 XRD patterns of $MgTi_2O_5$ nanoparticles synthesized by precipitation method

$$\delta = \frac{1}{L^2} \tag{3}$$

Values of L, δ, and ε for $MgTi_2O_5$ are obtained by the Scherer and Williamson-Hall treatments are shown in Table 2. Due to the elimination of the strain contribution to the FWHM of the XRD peak by W–H analysis, the crystallite size obtained by W–H analysis is slightly higher than that predicted using the Scherrer formula [33].

Various magnifications SEM images of $MgTi_2O_5$ nanoparticles prepared are shown in Fig. 4(a–c). SEM images show the interconnected spherical microstructure of $MgTi_2O_5$, which clearly shows the formation of spherical particles. The particle shapes are quasi-round and have the ability to combine, forming agglomerates of a few hundred nanometers in the 0.4–1.5 μm size range.

Figure 5(a and b) shows TEM images of $MgTi_2O_5$ nanoparticles at various magnifications. The $MgTi_2O_5$ nanoparticles are homogeneous, well distributed, quasi-round, and tend to aggregate and form clusters. The TEM images show that the $MgTi_2O_5$ nanoparticles are composed of nanoscale crystallites with an average size of around 30 nm. This value is quite close to the findings produced by W–H and Scherrer's approach. EDX analysis is used to verify the homogeneity of the resulting $MgTi_2O_5$ nanoparticles. The EDX spectrum of $MgTi_2O_5$ nanoparticles is shown in Fig. 6. The significant peaks in the spectrum corresponded to titanium, magnesium, and oxygen elements. Also, the metallic ratios of Ti, Mg, and O elements match well with the expected elemental ratio, which indicates that the synthesized nanoparticles are $MgTi_2O_5$.

The FT-IR spectra for $MgTi_2O_5$ nanoparticles are displayed in Fig. 7. The wideband at 3425 cm^{-1} is imputed to the stretching of the O–H group of water [36]. The intensive peak at 1630 cm^{-1} is due to the bending vibrations of H_2O particles [37]. The two bands at 1518 cm^{-1} and 1420 cm^{-1} are ascribed to the stretching vibrations of C–O and C–H, respectively [38]. The stretching of the O–H group of water is attributed to the wideband at 3425 cm^{-1} [36]. The bending vibrations of H_2O particles cause an intense peak at 1630 cm^{-1} [37]. The stretching vibrations of C–O and C–H are attributed to the two bands at 1518 cm^{-1} and 1420 cm^{-1}, respectively. The existence of bending vibrations of the intercalated Mg–O and Ti–O bonds is shown by the weak band at 500 cm^{-1} and the weak band at 605 cm^{-1} [38], respectively, demonstrating the development of a pure nanocomposite form of synthesized $MgTi_2O_5$.

Optical properties of $MgTi_2O_5$ nanoparticles

The optical properties of $MgTi_2O_5$ nanoparticles are studied using diffuse reflection spectra. Reflectance spectroscopy (RS) is utilized for powders that are difficult to analyze by transmission measurements. Reflectance measurements are divided into two categories: internal and exterior reflectance. To investigate the diffuse reflectance spectra that weakly absorbing materials produce, use the Kubelka–Munk hypothesis. The Kubelka–Munk equation for any wavelength is written as the following equation [39, 40]:

$$F(R) = \frac{(1-R)^2}{2R} \tag{4}$$

where R is the sample reflectance and F(R) is the Kubelka–Munk function. Figure 8 shows the diffuse reflectance of the $MgTi_2O_5$ nanoparticles. The synthesized $MgTi_2O_5$ nanoparticles absorbed mainly UV light, as shown in Fig. 9. The optical band gap E_g of $MgTi_2O_5$ can be calculated using a rewritten version of Tauc's equation [41–45] for diffuse reflectance calculations [40]:

Table 2 Structural characteristics of the $MgTi_2O_5$ nanoparticles

FWHM (rad) (10^{-2})	L (nm)		a (nm)	B (nm)	C (nm)	δ (10^{-3})	ε (10^{-3})
	Sch	WH					
0.2184	27.29	37.23	9.749	3.746	9.985	1.3458	0.9554

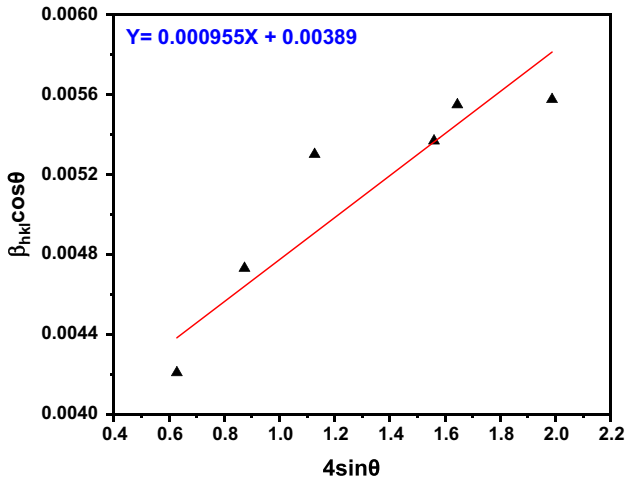

Fig. 3 Plotting of $\beta_{hkl}\cos\theta$ versus $4\sin\theta$

$$(\alpha h\nu) = \left(\frac{F(R)h\nu}{t}\right) = A(h\nu - E_g)^r \quad (5)$$

where α is the coefficient of absorption ($\alpha = F(R)h\nu/t$), $h\nu$ is the photon energy, t is the pellet thickness (approximately 0.5 mm), and r is a constant that defines the nature of optical transitions. Also, A is a constant known as the Tauc parameter that provides insight into the disorder in the sample [43–46], and its value may be calculated from the slope of the straight line. In the case of $MgTi_2O_5$, the best fit for Eq. (5) is obtained at r = 1/2, suggesting that the type of electronic transition is direct allowed transitions, which is demonstrated in Fig. 10. The value of E_g is determined from the intercept of the plot of $(F(R)h\nu/t)^2$ versus $h\nu$ for direct transition, as shown in Fig. 10 which is equal to 3.81 ± 0.01 eV. Moreover, the value of $A^{1/2}$ is equal to 776 ± 2 $(cm\ eV)^{1/2}$. The optical bandgap value of $MgTi_2O_5$ nanoparticles is matched with some previously reported work on their doped and thin-film materials [2, 12, 28, 47].

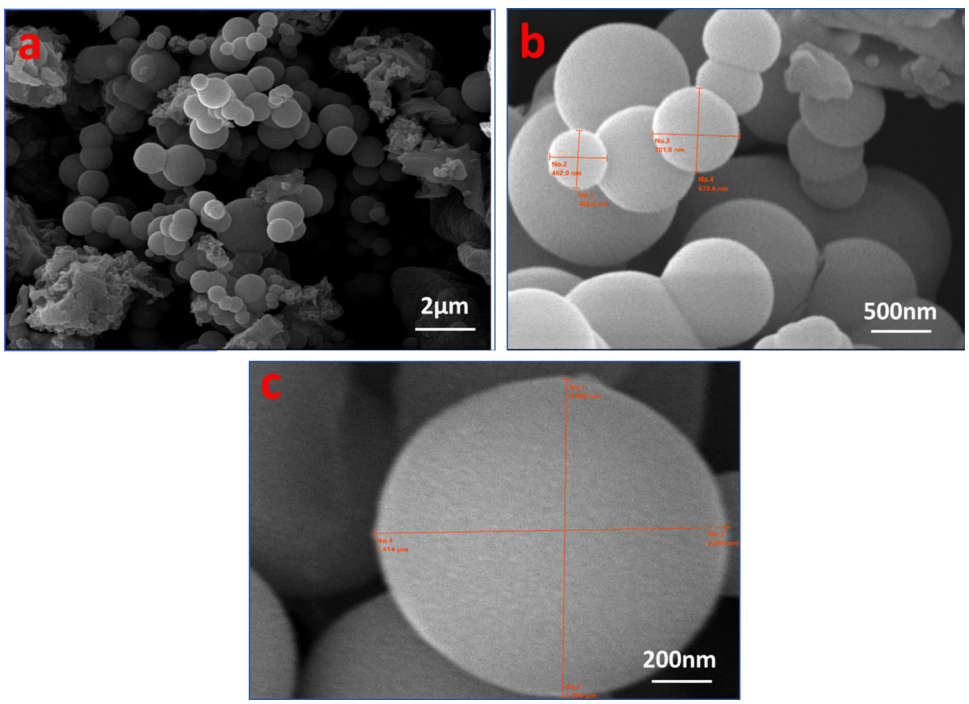

Fig. 4 SEM images of $MgTi_2O_5$ nanoparticle

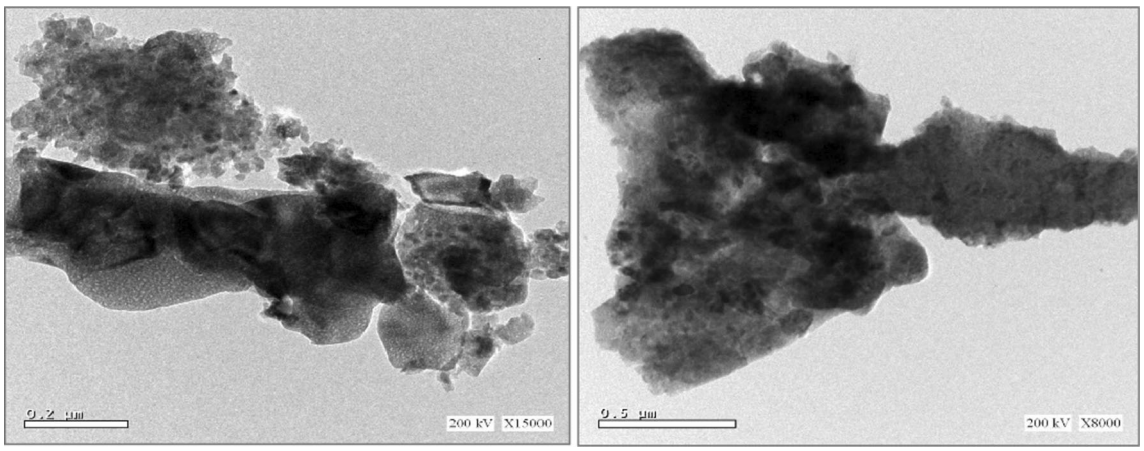

Fig. 5 TEM images of $MgTi_2O_5$ nanoparticles

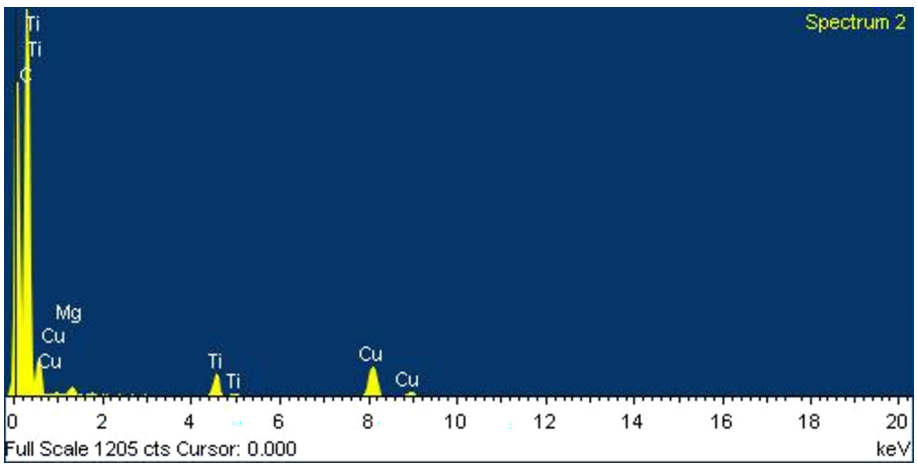

Fig. 6 EDX spectrum of $MgTi_2O_5$ nanoparticles

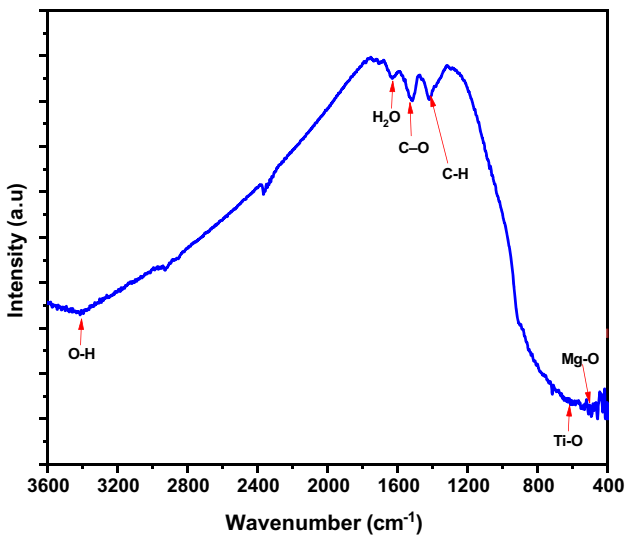

Fig. 7 FT-IR spectrum of $MgTi_2O_5$ nanoparticles

Electrical conductivity of $MgTi_2O_5$ nanoparticles

The electrical conductivity of the synthesized $MgTi_2O_5$ nanoparticles was investigated through the temperature-dependent conductivity within the range of temperature (303–503 K). Figure. 11 shows the DC electrical conductivity of the prepared $MgTi_2O_5$ nanoparticles. It is shown from Fig. 11 that the DC conductivity increases as temperature rises. The curve in Fig. 11 can be divided into three linear regions (1, 2, and 3). The electrical conductivity in these regions can be estimated by the following equation [39, 48, 49]:

$$\sigma_{dc} = \sigma_o \exp(-\Delta E_\sigma / K_B T) \quad (6)$$

where σ_{dc} is the dc electrical conductivity, σ_o is the electrical conductivity at zero temperature, k_B is Boltzmann's constant, ΔE_σ is the activation energy of the three regions, and T is the absolute temperature. From the slope and intercept of the straight lines of the curve, the variation in activation energy of $MgTi_2O_5$ nanoparticles for different temperature regions can be determined ($\Delta E_{\sigma 1}$, $\Delta E_{\sigma 2}$ and

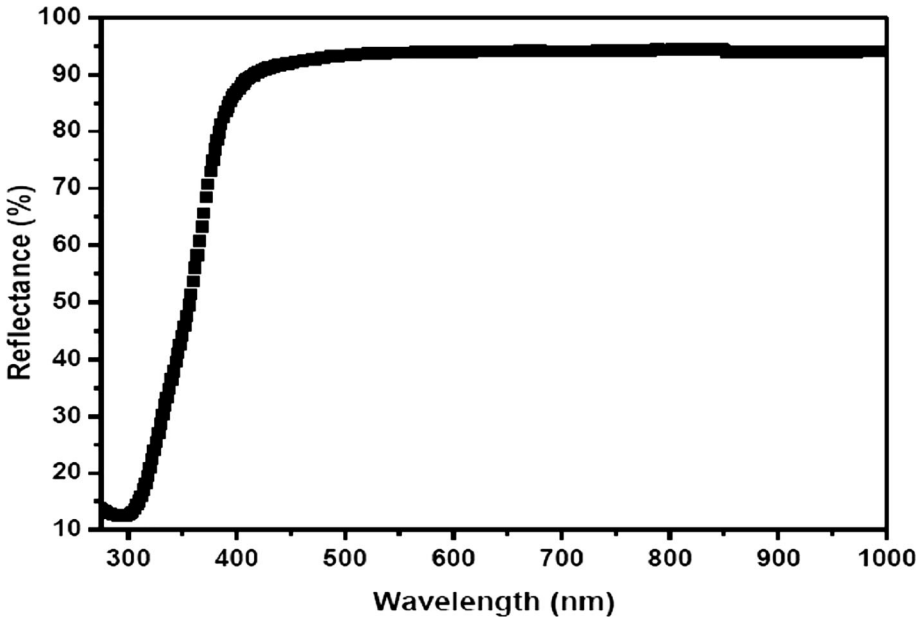

Fig. 8 The diffused reflectance versus wavelength for $MgTi_2O_5$ nanoparticles

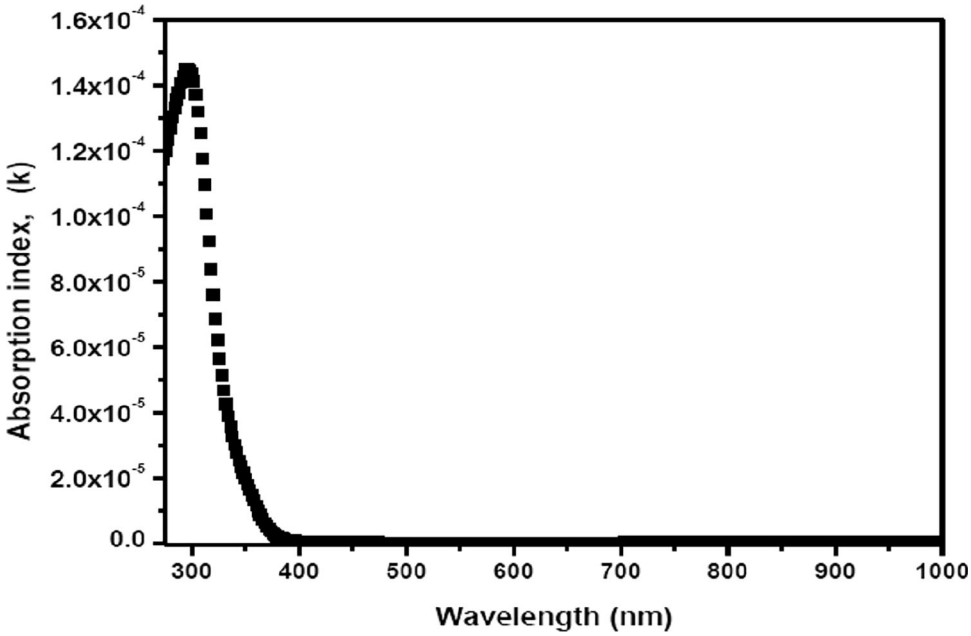

Fig. 9 Absorption index versus wavelength for $MgTi_2O_5$ nanoparticles

$\Delta E_{\sigma 3,}$ and σ_{o1}, σ_{o2}, and σ_{o3}). Estimated values for region (1) at the lower temperature range, region (2) at the intermediate temperature range, and region (3) at the higher temperature range are tabulated in Table 3, respectively. In intrinsic semiconductors, it is probable that the activation energy is less than half the value of the optical energy gap, which is already convenient with the determined values $\Delta E_{\sigma 1}$, $\Delta E_{\sigma 2,}$ and $\Delta E_{\sigma 3}$ for $MgTi_2O_5$ nanoparticles. The electrical study shows that the electrical conduction mechanism for the $MgTi_2O_5$ nanoparticles is thermally activated, and the DC conductivity enhances exponentially in the used temperature range (303–503 K), where the electrons are thermally excited from donor levels to the conduction band with temperature increasing. The determined values of the activation energy match the levels of defect energy in the optical bandgap of the $MgTi_2O_5$ nanoparticles. The results denote that these materials are promising for electronic device applications, as reported by previous researchers [49–52].

Antibacterial activity of $MgTi_2O_5$ nanoparticles

The present study examines the antibacterial properties of $MgTi_2O_5$ nanoparticles for the purpose of ensuring safety

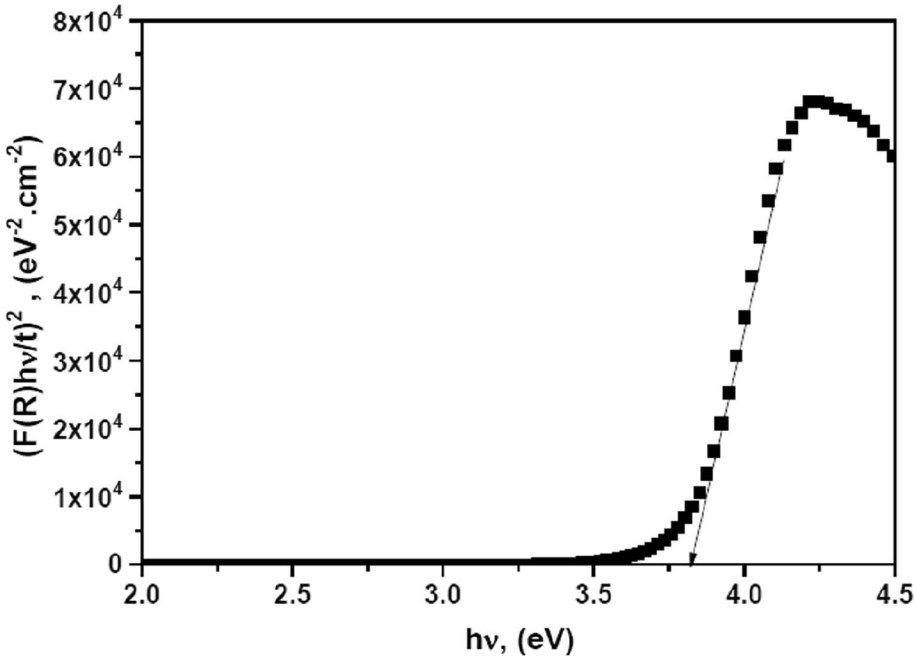

Fig. 10 Plotting of $(F(R)h\nu/t)^2$ versus the photon energy for $MgTi_2O_5$ nanoparticles

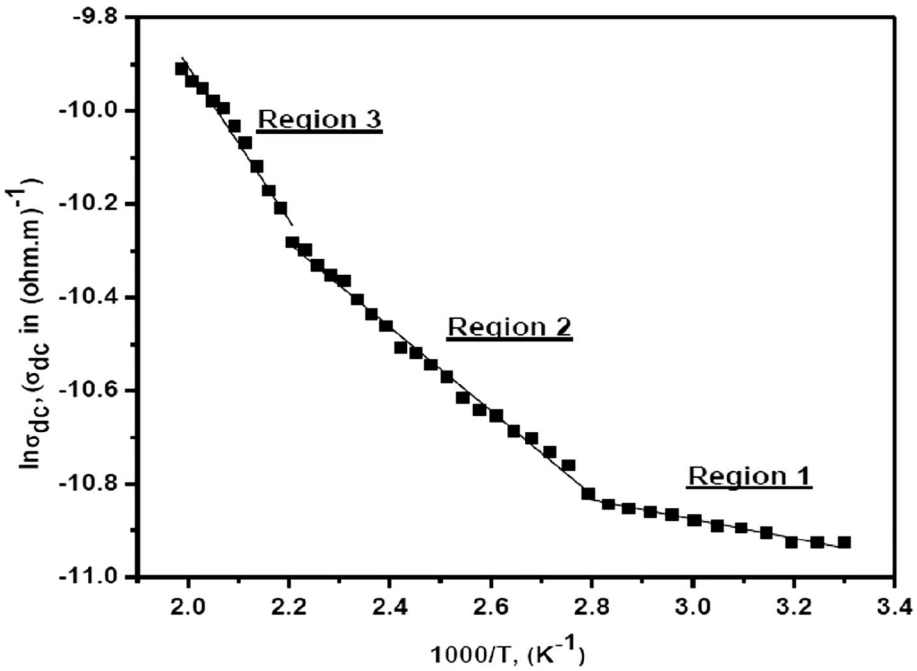

Fig. 11 Temperature dependent of the electrical conductivity of $MgTi_2O_5$ nanoparticles

Table 3 Activation energy values of $MgTi_2O_5$ nanoparticles for different temperature regions

Region	ΔE_σ (eV)	σ_o (Ohm m)$^{-1}$
1	0.018	3.52×10^{-5}
2	0.077	2.47×10^{-4}
3	0.142	1.34×10^{-3}

and promoting health. The minimum inhibitory concentration (MIC) is determined based on concentrations of nanoparticles impregnated onto sterile discs, as outlined in Table 1. The antibacterial activity of tested $MgTi_2O_5$ nanoparticles is determined by the existence of clear inhibition zones. It was seen that increasing the concentration of $MgTi_2O_5$ nanoparticles led to the inhibitory zone expanding faster. Different types of bacteria and different amounts of $MgTi_2O_5$ nanoparticles can cause the inhibitory zone to have different sizes. Table 4 presents the recorded

Table 4 Effect of the chemically synthesized compound on bacterial growth

Sample	Bacterial growth inhibition zone diameter (mm)	
Chloro-amphenicol (50 mg ml)	Gram (− ve) bacteria *E. Coli*	Gram (+ ve) bacteria *E. faecalis*
	11 ± 0.5	14 ± 0.4
	30	30

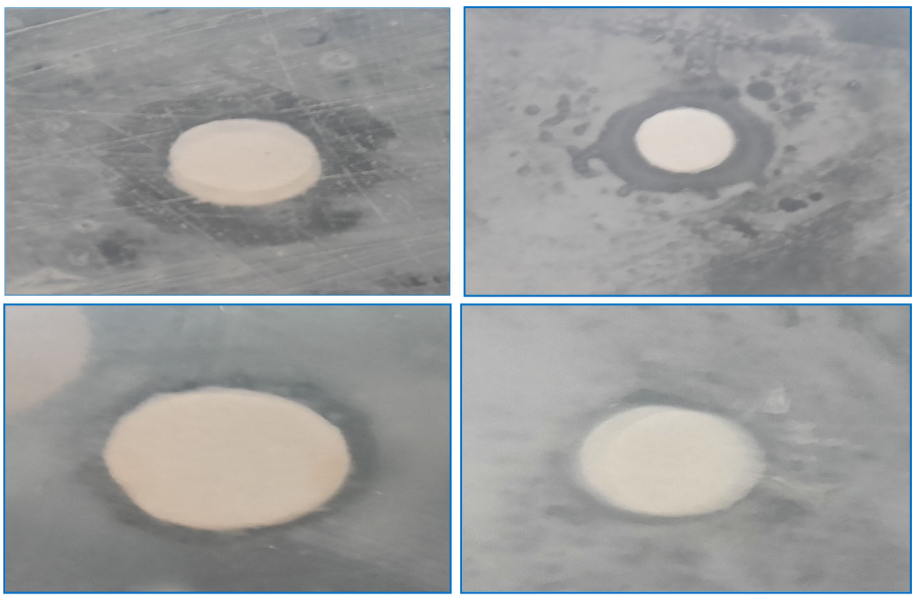

(a) **(b)**

Fig. 12 Inhibition zone of $MgTi_2O_5$ nanoparticles with both gram-positive and gram-negative. Bacterial strains (**a**) *E. coli* and (**b**) *E. faecalis*

values of the inhibitory zone for the bacterial strains employed in this study, namely *E. coli* and *E. faecalis*. The average values of the inhabitation zone often fall within the range of 10–15 mm. According to the data presented in Fig. 12 and Table 4, the observed highest growth inhibition zone for E. coli was 11 mm, whereas for *E. faecalis*, the maximum inhibition halo measured 14 mm. Hence, the findings pertaining to the antibacterial activity of $MgTi_2O_5$ indicate that the nanoparticles produced by $MgTi_2O_5$ exhibit notable efficacy in inhibiting bacterial growth.

$MgTi_2O_5$ nanoparticles' distinctive features make them interesting for antibacterial applications from a physics point of view. $MgTi_2O_5$ nanoparticles have a high surface-to-volume ratio, meaning they have a large surface area. This enormous surface area allows $MgTi_2O_5$ nanoparticles to interact with bacteria in several ways. Physical disruption of bacterial cell membranes is one way $MgTi_2O_5$ nanoparticles interact with bacteria. The sharp edges of $MgTi_2O_5$ nanoparticles may penetrate the cell membrane, leaking and killing germs. $MgTi_2O_5$ nanoparticles may interact with bacteria by generating reactive oxygen species (ROS). ROS are reactive chemicals that destroy microorganisms. $MgTi_2O_5$ nanoparticles create ROS through photocatalysis [53]. In addition to their antibacterial characteristics, $MgTi_2O_5$ nanoparticles offer additional antimicrobial benefits. Biocompatible $MgTi_2O_5$ nanoparticles are safe for living things. $MgTi_2O_5$ nanoparticles are cheap to create, making them a viable large-scale antibacterial contender.

Conclusions

Facile co-precipitation method was used to synthesis $MgTi_2O_5$ nanoparticles that have a structure similar to pseudobrookite. The synthesized $MgTi_2O_5$ nanoparticles were thermally analyzed using TGA and DSC. The crystallite sizes measured by the Scherer and W–H equations were in the 27–37 nm range. $MgTi_2O_5$ nanoparticles were found to have quasi-round forms in SEM and TEM images. The direct band gap (3.81 ± 0.01 eV) of the synthesized $MgTi_2O_5$ nanoparticles was investigated using diffuse

reflectance spectra. The temperature-dependent conductivity in the temperature range was used to study the DC electrical conductivity (303–503 K). These temperature-dependent measurements display that the electrical conduction mechanism for the $MgTi_2O_5$ nanoparticles was dominated by thermally activated processes. $MgTi_2O_5$ nanoparticles had excellent antibacterial capability and were effective against both gram-positive and gram-negative bacterial strains. Thus, it was concluded that the $MgTi_2O_5$ nanoparticles will be promising for antimicrobial applications and water purification.

Funding Open access funding provided by The Science, Technology & Innovation Funding Authority (STDF) in cooperation with The Egyptian Knowledge Bank (EKB). This research did not receive any specific grant from funding agencies in the public, commercial, or not-for-profit sectors.

Data availability This manuscript has associated data in a data repository. [Authors' comment: all data included in this manuscript are available upon request by contacting the corresponding author.]

Declarations

Conflict of interest The authors declare that there is no conflict of interest regarding the publication of this article.

References

[1] D N Haerani et al *Materialia* **27** 101692 (2023)
[2] H A Centurion et al *J. Alloys Compd.* **933** 167710 (2023)
[3] G Çelik and F Kurtuluş *Int. J. Mater. Res.* **106** 311 (2015)
[4] Y Suzuki and Y Shinoda *Sci. Technol. Adv. Mate.* **12** 034301 (2011)
[5] K Kornaus, P Rutkowski, R Lach and A Gubernat *J. Eur. Ceram.* **41** 1498 (2021)
[6] Y Wang, Y Xue, M Pan and S Wen *J. Alloys Compd.* **774** 222 (2019)
[7] H W Sona, Q Guoa, Y Suzuki, B N Kimd and T Mori *Scripta Materialia* **178** 44 (2020)
[8] M Rahman et al *J. Ind Eng. Chem.* **126** 340 (2023)
[9] T Selvamani, S Anandan, A M Asiri, P Maruthamuthu and M Ashokkumar *Ultrason. Sonochem.* **75** 105585 (2021)
[10] F Matteucci, G Cruciani, M Dondi, G Gasparotta and D M Tobaldi *J. Solid State Chem.* **180** 3196 (2007).
[11] T Lopez, J H Ventura, D H Aguilar and P Quintana *J. Nanosci. Nanotechnol.* **8** 6608 (2008)
[12] C H Lee and S I Kim *Integr. Ferroelectr.* **57** 1265 (2003)
[13] Y Nakagoshi and Y Suzuki *J. Asian Ceram. Soc.* **3** 334 (2015)
[14] X F Chen et al *Key Eng. Mater.* **538** 177 (2013).
[15] S Yoshikazu, T S Suzuki and Y Shinoda *Eng. Mater.* **14** 1134 (2012)
[16] Y Suzuki and M Morimoto *J. Ceram. Soc. Japan.* **118** 819 (2010)
[17] P N Kapoor, S Uma, S Rodriguez and K J Klabunde *J. Mol Catal A Chem.* **229** 145 (2005)
[18] J Bernard, D Houivet, J El Fallah and D Houivet *J. Eur. Ceram. Soc.* **24** 1877 (2004)
[19] Z A Aiken et al *Chem. Vap. Depos.* **16** 19 (2010)
[20] U Werapun and P Jaraslak *J. Nano Research* **56** 28 (2019)
[21] S Das et al *J. Alloys Compd.* **960** 170999 (2023)
[22] P Priyadarshini et al *Surf. Interfaces* **37** 102687 (2023)
[23] J H Mueller and J Hinton *Proc. Soc. Exp. Biol. Med.* **48** 330 (1941)
[24] A W Bauer, W M M Kirby, J C Sherris and M Turck *J. Clin. Pathol.* **45** 493 (1966)
[25] Z Ning et al *RSC Advances* **5** 106151 (2015)
[26] J Z Sun *Asian J. Chem.* **23** 1397 (2011)
[27] A R Lennie, K S Knight, C Michael and B Henderson *Am. Mineral.* **92** 1165 (2007)
[28] M A Ehsana, R Naeemb, V Mckeec, A S Hakeema and M Mazharb *Sol. Energy Mater. Sol. Cells* **161** 328 (2017)
[29] S Elnobi, M Dongol, T Soga and A A Abuelwafa *J. Alloys Compd.* **965** 171235 (2023)
[30] M S Ebied et al *J. Electron. Mater.* **51** 5770 (2022)
[31] H M Alsoghier et al *J. Mol. Struct.* **1179** 315 (2019)
[32] A A Abuelwafa, H M Alsoghier, S Elnobi, M Dongol and T Soga *Optik* **234** 166618 (2021)
[33] P Priyadarshini, S Das, D Alagarasan, R Ganesan, S Varadharajaperumal and R Naik *Scientifc Reports* **11** 21518 (2021)
[34] A A Abuelwafa, M S H Choudhury, M Dongol, M M El-Nahass and T Soga *J. Mater. Sci. Mater. Electron.* **29** 14232 (2018)
[35] S Das, S Senapati, G K Pradhan, S Varadharajanperumal and R Naik *ACS Appl. Nano Mater.* **6** 5298 (2023)
[36] T Ligia et al *Ceram. Int.* **40** 15693 (2014)
[37] E E Abdel-Hady, H F M Mohamed, M O Abdel-Hamed and M M Gomaa *Adv. Polym. Technol.* **37** 1 (2019)
[38] H Li et al *J. Nanopart. Res.* **13** 2117 (2011)
[39] C Aydn, M S Abd El-sadek, K Zheng, I S Yahia and F Yakuphanoglu *Opt. Laser Technol.* **48** 447 (2013)
[40] I S Yahia, H Y Zahran and F H Alamri *Synthetic Metals* **218** 19 (2016)
[41] H S Wasly, M S Abd El-Sadek, S Elnobi and A A Abuelwafa *Eur. Phys. J. Plus.* **137** 164 (2022)
[42] S Elnobi, M S Abd El-sadek, I S Yahia, H Y Zahran and A A Abuelwafa *J. Mater. Sci. Mater. Electron.* **33** 22092 (2022)
[43] P Priyadarshini, D Alagarasan, R Ganesan, S Varadharajaperumal and R Naik *CS Appl. Opt. Mater* **1** 55 (2023)
[44] D Sahoo et al *Indian J. Phys.* **96** 267 (2022)
[45] M Dongol, A F Elhady, M S Ebied and A A Abuelwafa *Indian J. Phys.* **95** 1245 (2021)
[46] F Gami, I Guizani, M A Sebak, A A Abuelwafa and M M Mostafa *Optical Materials* **134** 113093 (2022)
[47] P Gogoi, L R Singh and D Pamu *J. Am. Ceram Soc.* **101** 5389 (2018)
[48] M Dongol, A El-Denglawey, A F Elhady and A A Abuelwafa *Appl. Phys. A* **118** 34 (2015)
[49] A A Abuelwafa, S Elnobi, M A Santos and H M Alsoghier *Scientific Reports* **13** 12973 (2023)
[50] F Xie, Y Deng, Y Xie, H Xu and G Chen *Chem. Commun.* **51** 3545 (2015)

[51] A A Minea *Nanomaterials* **9** 1592 (2019)
[52] H Shin, H Shin, H S Jung, S Y Cho and K S Hong *Mater. Res. Bull.* **40** 2021 (2005)
[53] Z Jiang et al *Applied Catalysis B Environment* **257** 117898 (2019)